

Three-dimensional Deep-tissue Functional and Molecular Imaging by Integrated Photoacoustic, Ultrasound, and Angiographic Tomography (PAUSAT)

Muong Li

Duke University

Nathan Beaumont

SonoVol. Inc. <https://orcid.org/0000-0002-1135-5785>

Chenshuo Ma

Duke University

Juan Rojas

SonoVol, Inc.

Tri Vu

University at Buffalo, State University of New York

Max Harlacher

SonoVol. Inc.

Graeme O'Connell

SonoVol. Inc.

Ryan Gessner

SonoVol. Inc.

Hailey Kilian

University of Buffalo

Ludmila Kasatkina

Albert Einstein College of Medicine <https://orcid.org/0000-0003-3935-5389>

Yong Chen

Duke University

Qiang Huang

Duke University

Xiling Shen

Duke University <https://orcid.org/0000-0002-4978-3531>

Jonathan Lovell

University at Buffalo, State University of New York <https://orcid.org/0000-0002-9052-884X>

Vladislav Verkhusha

Albert Einstein College of Medicine

Tomek Czernuszewicz

SonoVol. Inc.

Junjie Yao (✉ junjie.yao@duke.edu)

Duke University <https://orcid.org/0000-0002-2381-706X>

Article

Keywords: deep-tissue imaging, photoacoustic imaging, ultrasound imaging, acoustic angiography, functional imaging, molecular imaging, photoswitchable protein

Posted Date: December 16th, 2021

DOI: <https://doi.org/10.21203/rs.3.rs-1143622/v1>

License:  This work is licensed under a Creative Commons Attribution 4.0 International License.

[Read Full License](#)

Version of Record: A version of this preprint was published at IEEE Transactions on Medical Imaging on January 1st, 2022. See the published version at <https://doi.org/10.1109/TMI.2022.3168859>.

1 **Three-dimensional Deep-tissue Functional and Molecular**
2 **Imaging by Integrated Photoacoustic, Ultrasound, and**
3 **Angiographic Tomography (PAUSAT)**

4 Mucong Li¹, Nathan Beaumont², Chenshuo Ma¹, Juan Rojas², Tri Vu¹, Max Harlacher², Graeme
5 O’Connell², Ryan C. Gessner², Hailey Kilian³, Ludmila A. Kasatkina⁴, Yong Chen¹, Qiang Huang¹,
6 Xiling Shen¹, Jonathan F. Lovell³, Vladislav V. Verkhusha⁴, Tomek J. Czernuszewicz^{2*}, Junjie Yao^{1*}

7
8 ¹Department of Biomedical Engineering, Duke University, Durham, NC 27708, USA

9 ²SonoVol, Inc., Research Triangle Park, Durham, NC 27713, USA

10 ³Department of Biomedical Engineering, University of Buffalo, State University of New York, Buffalo,
11 NY 14260, USA

12 ⁴Department of Anatomy and Structural Biology, and Gruss-Lipper Biophotonics Center, Albert Einstein
13 College of Medicine, Bronx, NY 10461, USA

14 *Correspondence to tomekc@sonovol.com, and junjie.yao@duke.edu

15 **Abstract:** Non-invasive small-animal imaging technologies, such as optical imaging, magnetic
16 resonance imaging and x-ray computed tomography, have enabled researchers to study normal
17 biological phenomena or disease progression in their native conditions. However, existing small-
18 animal imaging technologies often lack either the penetration capability for interrogating deep
19 tissues (*e.g.*, optical microscopy), or the functional and molecular sensitivity for tracking specific
20 activities (*e.g.*, magnetic resonance imaging). To achieve functional and molecular imaging in
21 deep tissues, we have developed an integrated photoacoustic, ultrasound and angiographic
22 tomography (PAUSAT) system by seamlessly combining light and ultrasound in a non-invasive
23 manner. PAUSAT can perform three imaging functions simultaneously with complementary
24 contrast: high-frequency B-mode ultrasound imaging of tissue morphology, microbubble-
25 enabled acoustic angiography of vasculature, and multi-spectral photoacoustic imaging of
26 molecular probes. PAUSAT can provide three-dimensional (3D) multi-contrast images that are
27 automatically co-registered, with high spatial resolutions at large depth. Using PAUSAT, we
28 conducted proof-of-concept *in vivo* experiments on various small animal models: monitoring
29 longitudinal development of placenta and embryo during mouse pregnancy, tracking
30 biodistribution and metabolism of near-infrared organic dye on the whole-body scale, and

31 detecting genetically-encoded breast tumor expressing photoswitchable phytochromes. These
32 results have collectively demonstrated that PAUSAT has broad applicability in biomedical
33 research, providing comprehensive structural, functional, and molecular imaging of small animal
34 models.

35 **Keywords** – deep-tissue imaging, photoacoustic imaging, ultrasound imaging, acoustic
36 angiography, functional imaging, molecular imaging, photoswitchable protein

37

38 **Introduction**

39 Non-invasive small-animal imaging technologies have evolved rapidly over the past decades
40 with increasingly broad applications, enabling researchers to study the progression of biological
41 events, evaluate the progression of various diseases, and monitor responses to treatment [1, 2].
42 All major medical imaging techniques such as x-ray computed tomography (CT), positron
43 emission tomography (PET) and magnetic resonance imaging (MRI), have been adapted for *in*
44 *vivo* small-animal imaging, usually with smaller formfactors and improved spatial resolutions
45 compared with their clinical counterparts [3-8]. Based on different contrasts, small-animal
46 imaging modalities can provide complementary information of the biological tissues. For
47 example, small-animal PET/CT maps tissue's morphology and metabolic activities with deep
48 penetration, but both PET and CT employ ionizing radiation, in addition to the poor soft tissue
49 contrast in CT and complicated workflow in PET, which hinders longitudinal studies [9-12].
50 Small-animal MRI uses non-ionizing radiofrequency waves to map soft tissue information with
51 excellent contrast and spatial resolution but suffers from a low imaging speed and high cost that
52 hamper some *in vivo* applications and limit throughput [1, 13]. To overcome the above
53 limitations, there need to be new imaging modalities that can provide non-ionizing functional
54 and molecular imaging in deep tissues.

55 While light is usually non-ionizing and intrinsically sensitive to tissue's functional and
56 molecular contrast, high-resolution optical imaging technologies such as multi-photon
57 microscopy often lack the penetration depth for deep tissue studies [14, 15]. Bioluminescence
58 and fluorescence imaging have also been widely applied for monitoring tumor development with
59 high sensitivity and contrast, but they suffer from poor spatial resolution at depths [16, 17].
60 Ultrasound tomography (UST), on the other hand, can provide deep tissue information with high
61 spatial and temporal resolutions, but so far still lacks molecular sensitivity [18-23]. Seamlessly

62 combining the rich optical absorption contrast and the deep ultrasound penetration, photoacoustic
63 tomography (PAT) is the promising optical imaging modality that can achieve functional and
64 molecular imaging at large depths with high spatial resolutions [24-26]. In PAT, the energy of
65 incident photons is absorbed by tissue chromophores and is partially or completely converted
66 into ultrasonic waves via non-radiative relaxation. The ultrasonic waves are subsequently
67 detected to reconstruct tomographic images of the original optical energy deposition in tissue [27,
68 28]. Because ultrasound waves are only weakly scattered in soft tissues, PAT can achieve high
69 spatial resolution at depths larger than 10 mm, far beyond the optical diffusion limit. Moreover,
70 due to optical absorption contrast, PAT has intrinsic functional and molecular sensitivity, which
71 is highly desired for preclinical research on small animal models. We have previously
72 demonstrated deep-tissue photoacoustic imaging of cancer metastasis with high sensitivity, using
73 near-infrared photoswitchable phytochromes [29]. Nevertheless, due to the lack of endogenous
74 contrast in the extravascular space, PAT typically cannot provide morphological information of
75 the soft tissue. Moreover, due to partial acoustic detection coverage and/or sparse spatial
76 sampling, PAT often suffers from streaking artifacts and missing structures.

77 High-performance small animal imaging needs high spatial resolution, high temporal
78 resolution, deep penetration, high structural fidelity, high throughput, and functional and
79 molecular sensitivity, all in the same system. None of the above imaging technologies can meet
80 this need alone, given their respective shortcomings. Therefore, it is most logical to integrate
81 multiple imaging modalities with complementary contrast mechanisms, compatible system
82 configurations, and comparable length scales. In this work, we report a technical advance in
83 small animal imaging: the integrated photoacoustic, ultrasound and angiographic tomography
84 (PAUSAT) platform. As a single imaging system, PAUSAT can provide comprehensive
85 information about organ structures via ultrasound imaging (US), vascular morphology via
86 acoustic angiography (AA), and molecular composition via photoacoustic imaging (PA) [30, 31].
87 All three imaging modes were engineered to function in the same system with shared scanning
88 mechanisms, synchronized controlling, and parallel signal detection. More importantly, the three
89 imaging modes share the same field of view and the images are automatically co-registered. We
90 have thoroughly characterized the performance of PAUSAT, and demonstrated its non-invasive
91 structural, functional, and molecular imaging with sub-millimeter resolutions at depths beyond
92 10 mm. PAUSAT has enabled multiple comprehensive small animal studies that are not feasible

93 by individual imaging modes, including longitudinal monitoring of placenta and embryo
94 development during mouse pregnancy, continuous tracking of biodistribution and metabolism of
95 a second-window near-infrared (1000 nm-1700 nm) organic dye on the whole-body scale, and
96 highly-sensitive detection of breast cancer expressing genetically-encoded photoswitchable
97 phytochrome. All these results have collectively demonstrated that PAUSAT is a powerful
98 imaging tool and may find a broad range of applications for basic research.

99 **Results**

100 **Configuration of the PAUSAT system.** The schematic and working principle of the PAUSAT
101 system is shown in **Figs. 1a-b**. PAUSAT was implemented from a modified Vega robotic
102 imaging system (SonoVol, Inc., Durham, NC), which employs two ultrasound transducers to
103 achieve the three imaging modes. The first transducer is a customized dual-element focused
104 wobbler, with a high-frequency inner element (35 MHz) and a low-frequency outer element (2
105 MHz). The two elements are concentrically aligned with a shared focal length. The second
106 transducer is a 128-element linear array (5 MHz) (L7-4, Philips, USA). The dual-element
107 focused transducer is used for US and AA imaging, providing high-resolution images of mouse
108 organ structures and vasculature perfusion at deep regions of interest. The US mode uses the
109 inner element for both high-frequency signal transmission and receiving. The AA mode uses the
110 outer element to burst microbubbles flowing in blood vessels and uses the inner element to
111 receive super-harmonic bubble bursting signals, resulting in high-contrast vasculature images
112 [32]. The linear array, coupled with a dual-branch optical fiber bundle flanking its lateral sides, is
113 used for the PA imaging to achieve high-speed molecular imaging with large penetration depth.
114 The excitation light source for the PA imaging is a pulsed Nd: YAG laser (Q-smart 850, Quantel
115 Laser, USA; wavelength: 1064 nm; pulse repetition rate: 10 Hz).

116 A FPGA based control box is programmed to synchronize the laser firing, motor stage
117 motion, and PA/US data acquisition. The US and AA signals are acquired by a single-channel
118 high-speed DAQ card. The PA signals are acquired by a programmable ultrasound scanner
119 (Vantage 256, Verasonics, USA). While the linear array provides axial cross-sectional images
120 for the PA mode with back-projection-based image reconstruction, the fast-scanning of the
121 wobbler provides axial cross-sectional images for the US and AA mode (**Supplementary Video**
122 **1**). The two transducers are mounted on a robotically actuated carriage with their relative
123 positions fixed. The carriage moves along a two-dimensional motorized stage for acquiring 3D

124 images with a large field of view [32]. The key acoustic, optical (except the laser), scanning, and
125 electrical components are fully immersed in a hydrocarbon fluid filled reservoir, which
126 improves the system's lubrication, acoustic coupling, and heat dissipation. The reservoir has an
127 optically and acoustically transparent imaging window on the top. The animal lies on the top of
128 the imaging window with a natural prone position, which can reduce the respiration-induced
129 motion artifacts.

130 **Characterization of PAUSAT.** We characterized the PAUSAT system's spatial resolutions as
131 shown in **Figs. 1c-d**. The cross-section of a carbon fiber ($\sim 7\ \mu\text{m}$ in diameter), representing a line
132 target, was imaged by the wobbler with the US mode and by the linear array with the PA mode.
133 The lateral resolution and axial resolution of the PA mode at 25 mm from the linear array surface
134 were $412.5\ \mu\text{m}$ and $418.7\ \mu\text{m}$, respectively. The US mode had an axial resolution of $118.7\ \mu\text{m}$
135 and a lateral resolution of $206.9\ \mu\text{m}$, which are close to the theoretical values. The spatial
136 resolutions of the AA mode should be slightly worse than the US mode, since the same wobbler
137 is used but the AA mode only involves one-way ultrasound focusing. The wobbler can also work
138 at different frequencies, resulting in different spatial resolutions and penetration depths, due to
139 the frequency-dependent attenuation of ultrasound waves. As shown in **Fig. 1e**, cross-sectional
140 US images of a pregnant mouse were acquired at three transmission frequencies of 15 MHz, 25
141 MHz and 35 MHz. High-frequency US images provide better spatial resolution but smaller
142 penetration depth.

143 **Validation of the PAUSAT system on phantoms.** The three imaging modes in PAUSAT
144 provide complementary information of the same target. We first validated the imaging
145 performance of PAUSAT by imaging a knot phantom made of a soft tube (inner diameter, $200\ \mu\text{m}$;
146 outer diameter $300\ \mu\text{m}$) to mimic a blood vessel. The tube was perfused with water,
147 microbubbles, or an NIR-II dye BIBDAH for the US, AA and PA mode, respectively. All three
148 imaging modes were able to delineate the shape of the knot based on different contrasts, as
149 shown in **Fig. 2a**. The US image provides a sharp image of the tube wall, however, also shows
150 the imaging window membrane which the tube is resting on. AA mode displays similar
151 resolution; however, it exhibits almost no background signal and, consequently, high contrast of
152 the tube lumen. The PA mode has worse resolution than the US and AA mode, due to the weak
153 elevational focusing of the linear array and lower ultrasonic center frequency. The cross-
154 sectional images are shown in **Fig. 2b**, with the axial and lateral profiles shown in **Fig. 2c**. In the

155 axial direction, the US image shows both top and bottom walls of the tube, while the PA and AA
156 images show the lumen of the tube.

157 Although the PA mode can be used for vascular imaging with hemoglobin as the endogenous
158 contrast [33-35], the AA mode can provide vascular images with better contrast and resolution.
159 On the other hand, the PA mode has the unique molecular sensitivity with a variety of exogenous
160 contrast agents [36-38], which cannot be provided by the US or AA mode. Here we tested the
161 molecular imaging of the PA mode using an NIR-II BIBDAH dye that has strong optical
162 absorption at 1064 nm. **Figure 2d** shows the PA images of BIBDAH-filled tubes with different
163 concentrations. The quantitative results in **Fig. 2e** show that the PA signal amplitude is
164 proportional to the dye concentration, which is the foundation for spectroscopic PA measurement.
165 The PA signals of whole bovine blood were also acquired at 1064 nm, which were comparable to
166 that of the BIBDAH dye with a 50 $\mu\text{g}/\text{mL}$ concentration. The strong PA performance of
167 BIBDAH dye is consistent with the optical absorption spectra of the BIBDAH dye and blood in
168 **Fig. 2f** [39].

169 **PAUSAT validation on small animals.** To further validate the system for *in vivo* small animal
170 studies, a mouse model was developed by subcutaneously implanting an artificial Matrigel
171 “tumor” mixed with the BIBDAH dye (no tumor cells included) close to the liver cavity as
172 shown in **Fig. 3a**, mimicking the targeted exogenous PA contrast agents tagging tumor cells [40].
173 The PA, US, and AA modes were then used sequentially to scan the artificial tumor region.
174 **Figure 3b** shows the maximum amplitude projection images along the elevational direction. The
175 artificial tumor was clearly imaged by the US mode as a hypoechogenic mass with a contrast to
176 noise ratio (CNR) of 3.01, since the Matrigel had low acoustic reflectivity [41]. The AA mode
177 provided abundant vascular network around the tumor implant but was not able to clearly
178 delineate the tumor region. The PA image highlighted the strongest BIBDAH signals from the
179 tumor region with a CNR of 14.38, much better than the US image. The complementary nature
180 of the three imaging modes can be more clearly visualized from the coronal cross-sectional
181 images shown in **Fig. 3c**. The liver region was located by the US image, and the AA image
182 provided the fine vascular architecture of the liver. The PA image highlighted the tumor implant.
183 **Figure 3d** shows the 3D rendering of the merged images combining the three imaging modalities
184 (**Supplementary Video 2**). **Figure 3e** further shows the superimposed images of the US, AA

185 and PA modes, illustrating the relative positions of the liver, the hepatic blood vasculature and
186 the artificial tumor.

187 **Longitudinal imaging of the mouse pregnancy.** Non-invasive imaging of the developing
188 embryo *in vivo* with normal pregnant conditions is highly desired for developmental biology and
189 reproductive science. Traditional optical imaging cannot clearly visualize the deep-seated
190 embryos without implanting intravital windows which are invasive and may lead to embryo
191 death [42]. PAUSAT was then used for longitudinal non-invasive imaging of *in vivo* mouse
192 pregnancy to solve this issue. In this experiment, the developing embryos and placenta were
193 imaged by the US mode (**Fig. 4a**) and the PA mode (**Fig. 4d**) every two days from E9 to E17,
194 and by the AA mode (**Fig. 4e**) at E9, E13 and E17. The development of a representative embryo
195 over the 9 days is shown in the close-up US images in **Fig. 4b** and **Supplementary Video 3**. The
196 embryonic body part such as the head, the spinal cord and the tail were clearly resolved. The
197 crown-rump length (CRL), which is the length of the embryo from the top of its head to the
198 bottom torso, is an important clinical parameter to estimate the embryo's gestation age (GA) [43].
199 We measured the CRL values of the visible embryos at each imaged gestation age from the US
200 images (**Fig. 4c**). A linear fitting was performed to show the growth rate of the embryos. To
201 verify the accuracy of the CRL measurements, we adapted a CRL prediction model describing
202 the change of the CRL with GA as $CRL = -9.42 + 1.09(GA) + 0.0281(GA)^2$ [43]. From both our
203 US measurements and predictions model, it can be observed that CRL increased approximately
204 linearly with the gestation age. **Figure 4d** and **Supplementary Video 4** show the PA images of
205 the mother mouse at the abdominal area. The green dotted lines indicate the same landmark
206 blood vessels at different time points. The same embryo can then be located from the PA images
207 based on the landmark vessels as indicated by the green rectangles. In the AA images in **Fig. 4e**
208 and **Supplementary Video 5**, we can clearly visualize blood vessels in the maternal organs, as
209 well as the placentas since E13. The embryos were not visible in the AA mode because the
210 microbubbles could not pass the placental barrier [44]. The three-dimensional AA images are
211 shown in **Supplementary Video 6**. In addition, since the placental size is an indicator of fetal
212 development and pregnancy outcome, we measured placental diameter (PD) and placental
213 thickness (PT) in the US and AA images for all the embryos at E11, E13 and E15, where the
214 placentas were well identified. The measured placental sizes at these gestation age agreed with

215 the predicting models as $PD = -11.96 + 2.09(GA) - 0.046(GA)^2 - 0.0005(GA)^3$ and $PT = 4.10 -$
216 $1.14(GA) + 0.115(GA)^2 - 0.0031(GA)^3$ [43].

217 **Tracking the biodistribution of an NIR-II dye.** It is critically important to monitor the
218 biodistribution and metabolism of organic chemicals at the whole-body level for drug
219 development and treatment evaluation. PAUSAT is fully capable of molecular imaging with high
220 detection sensitivity. As a proof of concept, we demonstrated the application of PAUSAT for
221 monitoring the metabolism of a BIBDAH dye in a mouse. The coronal PA images of the mouse
222 before and after administrating BIBDAH via the tail vein are shown in **Fig. 5a**. A clear increase
223 in the PA signal strength was observed in the major blood vessels right after the dye injection.
224 The PA signal of the dye at 0.1 mg/mL was ~5 times higher than that of the blood. The blood
225 vessels imaged by the PA mode were mostly detected along the elevational direction, while
226 much fewer vessels were detected along the lateral direction, since PA signals generated from
227 blood vessels are strongly orientation dependent [45]. The PA signals from the lateral blood
228 vessels were not detected by the full aperture of the linear transducer array, which resulted in
229 their low visibility. Within 4 hours, the PA signals increased by 5 times in the liver, indicating
230 that the dye was accumulated in the liver, consistent with previous results [36]. **Figure 5b** shows
231 representative cross-sectional images of the liver region acquired at three time points. The
232 images are shown in a logarithmic scale to highlight deeper signals. These results show that the
233 penetration depth of the PA mode was improved after injecting the dye, as marked by the white
234 dotted circle. **Figure 5c** shows the PA signal dynamics from the major blood vessels in the skin
235 and from the liver. The 3D superimposed PA and US image of the liver region is shown in **Fig.**
236 **5d**. The PA signals in the liver continuously increased over four hours, showing the
237 accumulation of dye in the liver. By contrast, the PA signals in the skin blood vessels reached a
238 plateau one hour after injection. The persistent dye signals in the blood vessels are due to the
239 relatively high concentration of dye. The slow clearance of the dye from the blood stream to the
240 liver did not affect the PA signals in the blood vessels.

241 **Detecting reversibly-photoswitching tumors.** In addition to exogenous organic dyes,
242 endogenous genetic reporters, such as reversibly photoswitchable phytochromes, have become
243 increasingly popular in PA molecular imaging due to their high biocompatibility and much
244 enhanced detection sensitivity. One of these phytochrome proteins is *Bphp1* that originates from
245 rhodospseudomonas [29, 46]. From the optical absorption spectra in **Fig. 6a**, *Bphp1* exhibits two

246 switchable absorbing states: the Pfr state and the Pr state. The Pfr state is the ground state or ON
247 state. With 730-790 nm optical illumination, *BphP1* undergoes photoconversion to its Pr state or
248 OFF state, at which the optical absorption is shifted to 630-690 nm. The molar extinction
249 coefficient of *Bphp1* at the ON state (at 750 nm) is ~70 times higher than that of oxygenated
250 hemoglobin [29]. This photoswitching is reversible between the two states. In this experiment,
251 we implanted transgenic *Bphp1*-expressing 4T1 tumor cells into the mouse flanks and imaged
252 the tumor regions after three weeks with US, AA, and PA modes. For PA imaging, we used a
253 750-nm pulsed laser to both generate PA signals and switch off *Bphp1*, and a 635-nm CW laser
254 to switch the proteins back on (**Fig. 6b**). Axial-view US and AA images are shown in **Fig. 6c**,
255 with the two tumor locations identified. The tumors showed low echogenicity in the US image,
256 and no noticeable increase in blood perfusion was observed inside the tumors from the AA
257 image. The PA images of the tumors acquired with *Bphp1* at the ON and OFF states were
258 dominated by the background signals from hemoglobin (**Fig. 6d**). By contrast, the differential
259 PA image between the ON and OFF state can clearly detect the tumor signals with the
260 background hemoglobin signals effectively suppressed (**Fig. 6e**). The differential PA image was
261 then compared with the US image (**Fig. 6f**), and the *Bphp1*-expressing tumor locations
262 correspond well with the US-detected tumor positions. Representative PA signals from the tumor
263 and background over several switching cycles are shown in **Fig. 6g**, in which repeatable
264 photoswitching was observed from the tumors but not from the blood.

265 **Discussion**

266 In this work, we have presented a 3D non-invasive small-animal imaging system that
267 combines photoacoustic, ultrasound, and acoustic angiography imaging in a single device.
268 PAUSAT can provide complementary information about biological tissues: structural
269 information with US mode, vascular information with AA mode, and molecular information with
270 PA mode. We performed *in vitro* studies to characterize the system and showed that high spatial
271 resolutions are achieved by all three imaging modes for deep tissues. We also demonstrated the
272 system's *in vivo* performance in various proof-of-concept small animal studies, including
273 longitudinal monitoring of mouse pregnancy, tracking the biodistribution of an NIR-II dye, and
274 detecting reversible photoswitching tumors. All the results collectively show the flexibility and

275 versatility of the PAUSAT system for small animal studies, and potential wide applicability in a
276 variety of basic research.

277 Compared with the US and AA mode that use high-frequency ultrasound, the PA mode has
278 worse lateral and axial resolutions, which can be further improved by using an ultrasound array
279 with a higher central frequency and broader bandwidth. The elevational resolution of the PA
280 mode is limited by the elevational focusing, which can be improved by changing the scanning
281 geometry or applying advanced 3D reconstruction algorithms [47-49]. The penetration depth of
282 the US and AA mode is scalable, depending on the transmission ultrasound frequency. The
283 penetration depth of the PA mode is fundamentally limited by the optical attenuation of the
284 tissue, and can be improved by illuminating the mouse from multiple angles [50].

285 Another limitation of the current PAUSAT system is that two ultrasound transducers are used
286 for three imaging modes that have increased the complexity in the image co-registration and
287 prevented acquiring all three images simultaneously. While the US and AA modes share the
288 same ultrasound transducer and therefore are naturally registered, the PA mode needs to be co-
289 registered with the US and AA mode using geometric information of the two transducers.
290 Geometric registration works well given stationary of the imaging subject, however if the animal
291 moves between scans (e.g., muscle spasm, incomplete anesthesia) registration fidelity may
292 decrease. Another method to register images from different modalities is matching the blood
293 vessels from both AA and PA images with non-rigid registration techniques [51]. Artificial
294 markers attached to the animal that can be imaged by all three imaging modes could also be used
295 to achieve more precise image registration.

296 The stock concentration of microbubble used in the AA mode is 2×10^9 bubbles/ml. The
297 relatively high microbubble concentration is necessary due to the passive bubble clearance in the
298 blood stream and the active bubble bursting by the ultrasound pulses. Previous studies have
299 shown that without active bursting, the lifetime of microbubbles in the blood stream depends on
300 the bubble size. Microbubbles with a diameter of 1 μm can last for ~5 mins in the blood
301 circulation before the bubble signals drop to the background level [52, 53]. In our study, we used
302 a size-sorting process to produce larger microbubbles with a diameter of 5 μm that could last
303 longer in the circulation system and thus allow a longer imaging time window [54]. Nevertheless,
304 the AA mode actively burst the bubbles to generate high-frequency harmonic signals, which
305 accelerates the bubble clearance rate. Also, in our current setting, the AA mode averages

306 multiple repeated frames at each location in order to improve the contrast of the major blood
307 vessels, which, can suppress the signals from small vessels, especially capillaries with low flow
308 speed. This multi-frame averaging further speeds up the microbubble clearance. Ultimately, we
309 have an average microbubble lifetime of ~20 mins in the blood circulation, which is sufficient to
310 cover a field of view of 20 mm by 40 mm. Reducing the frame averaging can prolong the bubble
311 lifetime at the price of image contrast. An alternative approach to maintain a longer bubble
312 circulation time is to use a continuous infusion pump by placing a catheter into the vein.

313 In the pregnant mouse imaging (**Fig. 4**), the major organs of the mouse embryos can be well
314 resolved with the US mode and the maternal blood vasculature can be seen with the AA mode.
315 While microbubbles are considered safe for *in vivo* imaging, the active bubble bursting may be a
316 safety concern [55, 56]. The bubble busting may generate high-pressure micro-streams that can
317 change the permeability of the syncytiotrophoblast, which is the maternal-embryo exchange
318 interface and a protective barrier [44, 57]. Previous studies on the blood-brain barrier have
319 shown that this bubble-induced effect on the barrier permeability is transient, if present [58]. In
320 our experiments, we did not observe any adverse effects on the maternal and embryo functions
321 over the gestation period after the start of imaging. The US images confirmed the normal
322 progress of pregnancy up to the delivery. We also noticed that the embryos were generally
323 invisible in the AA images, indicating that the microbubbles could not cross the placental barrier
324 and therefore the risk of barrier permeability was low. The PA mode could not provide clear
325 coronal images of the embryos because it was limited by the elevational resolution; however, PA
326 mode may be used for other functional studies of mouse pregnancy, such as fetal oxygenation
327 measurement and drug delivery monitoring [59-61].

328 From the US and AA images in **Fig. 4**, we can see half-moon-shaped organs close to the
329 embryos. Since mature mouse placentas are established around mid-gestation (~E10.5) [62],
330 these observed organs are most likely decidua before E10.5 and placentas afterwards. The basal
331 decidua becomes progressively thinner over the pregnancy while placental villi within the
332 labyrinth zones proliferate rapidly [63, 64]. The AA signals of the placenta were weaker at E17,
333 probably because the placentas were pushed to deeper regions with the developing embryos. The
334 imaging depth of the AA mode can be improved by using microbubbles with smaller diameters,
335 which can lower the pressure threshold needed to burst the bubbles in deep tissues [65, 66]. The
336 weaker placenta signals in PA images at E17 are likely due to the insufficient light penetration

337 depth. Again, improving the light illumination geometry can help increase the imaging depth of
338 the PA mode.

339

340 **Acknowledgement:** We thank Dr. Caroline Connor for editing the manuscript and Kun Xiang
341 for technical support and useful discussion on animal experiments. This work was sponsored by
342 National Institutes of Health (R01 EB028143, R01 NS111039, RF1 NS115581, R21 EB027304,
343 R21EB027981, R43 CA243822, R43 CA239830, R44 HL138185); American Heart Association
344 Collaborative Sciences Award (18CSA34080277); Chan Zuckerberg Initiative Grant on Deep
345 Tissue Imaging 2020-226178 by Silicon Valley Community Foundation; All to J.Y.

346 **Author contributions:** J.Y., T.C. and R.G. conceptualized the study and oversaw the whole
347 project. M.H. and G.O. constructed the hardware of US and AA modes. M.L. constructed the
348 hardware of PA mode. N.B. and T.V. wrote software and synchronization sequences. C.M.
349 contributed to the pregnant mouse experiment and photoswitching experiment. J.R. processed the
350 AA and US images for small animal validation experiment. H.K. and J.L. developed the
351 BIBDAH dye. L.K. and V.V. developed the photoswitching cell lines. Y.C., Q.H. and X.S.
352 developed the pregnant mice. M.L. performed all the other experiments, processed the data and
353 images. M.L. and J.Y. wrote the manuscript. N.B., M.H., G.O., J.R. T.C. and R.G. edited the
354 manuscript.

355

356 **Online Methods:**

357 **PAUSAT scanning configuration:** In the US and AA mode, a field of view of ~40 mm by 20
358 mm (lateral by elevational) was scanned by the wobbler with a scanning step size of 0.2 mm
359 along the elevational dimension and the pixel size is 0.05 mm along the lateral dimension. The
360 width of the wobbler field of view is ~17 mm and therefore 3 passes were taken and stitched to
361 span 40 mm. In the AA mode, the lateral scanning was repeated 5 times and averaged to enhance
362 the image quality. It took ~ 5 min to acquire a 3D volumetric US data and 30 min for a 3D AA
363 data. For the US and AA mode, 3D images were reconstructed using a pixel-based volume
364 reconstruction method and compounding for overlapped pixels [67]. In PA mode, the linear array
365 was scanned elevationally with a step size of 0.2 mm and a scanning length of 40 mm. Five
366 repeated frames are taken at each location for averaging. It took ~5 mins to acquire a 3D PA data.
367 The optical pulse energy from the fiber output was ~ 20 mJ at 1064 nm, with a spot size of 10

368 mm by 40 mm on the sample surface. The axial cross-sectional PA images were reconstructed in
369 real time and 3D rendering images were processed offline using Matlab. For the PA mode, the
370 back-projection reconstruction method was performed for each cross-sectional image [68, 69].

371 **Phantom preparation:** In the AA result in **Fig. 2(a)**, microbubbles (Sonovol, Inc.; Diameter: 5
372 μm) were infused into the plastic tube (inner diameter, 200 μm ; outer diameter 300 μm) at the
373 rate of 1×10^8 bubbles/min continuously with a catheter, which was driven by an automatic
374 syringe pump to mimic the blood circulation. In the PA results of **Fig. 2(d)**, the lab-made
375 BIBDAH dye was prepared with four different concentrations (0.5 mg/mL, 0.2 mg/mL, 0.1
376 mg/mL, 0.05 mg/mL) diluted with PBS [36]. The dye solutions were injected into transparent
377 plastic tubes (inner diameter: 200 μm ; outer diameter: 300 μm). A fifth tube was filled with
378 whole bovine blood (Quad Five, Inc.). The tubes were sandwiched by two pieces of thin agar
379 sheets and placed on top of the imaging window of the PAUSAT system. The imaging window
380 was then covered by a thin layer of distilled water as the ultrasound coupling medium.

381 **Animal preparation:** The protocol of all the animal experiments was proved by the institutional
382 animal care and use committee of Duke University. Female BALB/c mice (8 weeks old; 20-30
383 grams in weight) were used for all experiments. The hair on the mouse chest, abdomen or back
384 was shaved and depilated as needed. The mice were then anesthetized with 1.5% v/v isoflurane
385 and placed on the imaging window of the PAUSAT system with a 1-mm-thick agar pad
386 underneath. This agar pad served as a spacer to separate the PA and US signals from the mouse
387 skin surface and the imaging window membrane. Water was used to couple the membrane, the
388 agar pad and the mouse skin. A heating lamp was used to maintain mouse body temperature at
389 37°C . For all the AA imaging, a total of 200 μL microbubbles with the concentration of 2×10^9
390 /ml were injected via the tail vein with a 27-gauge syringe. For the PA liver imaging shown in
391 **Fig. 3**, Matrigel mixed with the BIBDAH dye was implanted around the liver region
392 subcutaneously to create an artificial tumor with a volume of 15 mm^3 . For PA dye metabolism
393 imaging shown in **Fig. 5**, 200 μL BIBDAH dye with the concentration of 0.5 mg/mL was
394 injected via the tail vein, and the PA imaging were performed every hour.

395 **Pregnant mouse preparation:** CD-1 IGS mice of ~8 weeks old were used for timed breeding by
396 checking vaginal plugs. To prepare the pregnant mice, female mice at the proestrus phase were
397 placed together with male mice for mating. The females were then checked in the following

398 morning at 8-9 am for vaginal plug. When a plug was seen, they were separated and the day
399 when the plug was found was considered as the first day of gestation. The embryos were also
400 staged in days of gestation, and the morning when the vaginal plug was detected was defined as
401 E0.5. The pregnant mice were imaged from E8.5.

402 **Photoswitching imaging:** *Bphp1*-expressing 4T1 cells were grown in DMEM supplemented
403 with 10% FBS and 1% penicillin-streptomycin mixture at 37 °C in 5% CO₂ atmosphere. The
404 BALB/c mouse was placed under anesthesia with 1.5% isoflurane and *BphP1*-expressing 4T1
405 cells (4×10^4) were injected subcutaneously under the 4th mammary fat pad. The mouse was
406 imaged when the tumor diameter was ~5 mm, as measured by calipers. For all photoswitching
407 studies, the switching settings were the same. A total of 8s of 635 nm CW light was used for
408 switching on the Bphp1 protein, followed by a total of 8s of 750nm pulse light for both PA
409 imaging and switching off the protein. We acquired 24 switching cycles and averaged the images
410 accordingly. The differential images were obtained by subtracting the OFF-state images from the
411 ON-state images [29, 70].

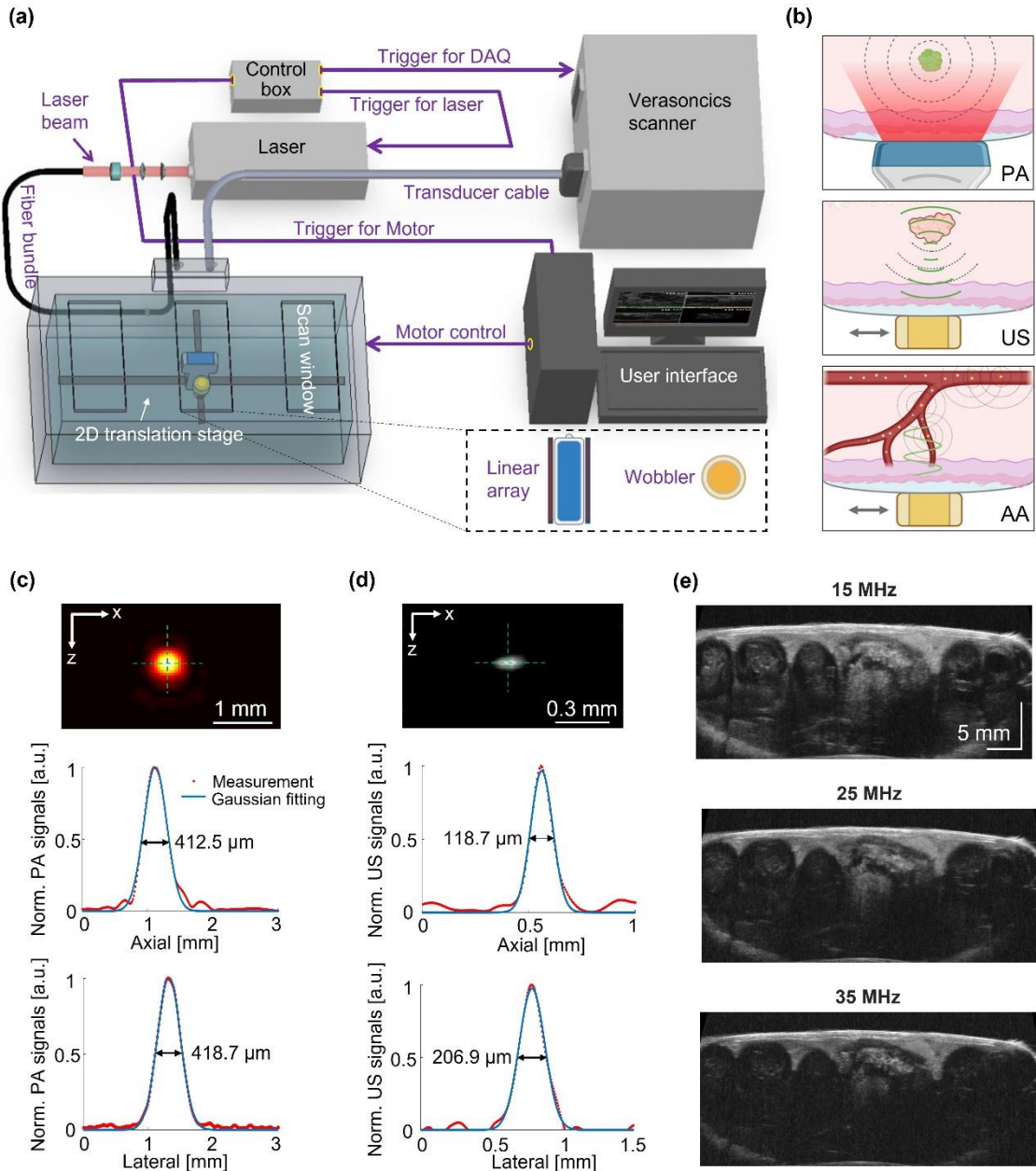
412 **References**

- 413 1. Cunha, L., et al., *Preclinical imaging: an essential ally in modern biosciences*. Mol Diagn Ther,
414 2014. **18**(2): p. 153-73.
- 415 2. Lewis, J.S., et al., *Small animal imaging. current technology and perspectives for oncological*
416 *imaging*. Eur J Cancer, 2002. **38**(16): p. 2173-88.
- 417 3. Pandit, P., et al., *The utility of micro-CT and MRI in the assessment of longitudinal growth of liver*
418 *metastases in a preclinical model of colon carcinoma*. Acad Radiol, 2013. **20**(4): p. 430-9.
- 419 4. Vaquero, J.J. and P. Kinahan, *Positron Emission Tomography: Current Challenges and*
420 *Opportunities for Technological Advances in Clinical and Preclinical Imaging Systems*. Annu Rev
421 Biomed Eng, 2015. **17**: p. 385-414.
- 422 5. Hutchinson, J.C., et al., *Early clinical applications for imaging at microscopic detail: microfocus*
423 *computed tomography (micro-CT)*. British Journal of Radiology, 2017. **90**(1075).
- 424 6. Jiang, Y., et al., *Micro CT and Micro MR imaging of 3D architecture of animal skeleton*. J
425 Musculoskelet Neuronal Interact, 2000. **1**(1): p. 45-51.
- 426 7. Ashton, J.R., J.L. West, and C.T. Badea, *In vivo small animal micro-CT using nanoparticle contrast*
427 *agents*. Frontiers in Pharmacology, 2015. **6**.
- 428 8. Judenhofer, M.S. and S.R. Cherry, *Applications for preclinical PET/MRI*. Semin Nucl Med, 2013.
429 **43**(1): p. 19-29.
- 430 9. Lee, C.L., et al., *Assessing cardiac injury in mice with dual energy-microCT, 4D-microCT, and*
431 *microSPECT imaging after partial heart irradiation*. Int J Radiat Oncol Biol Phys, 2014. **88**(3): p.
432 686-93.
- 433 10. Clark, D.P. and C.T. Badea, *Micro-CT of rodents: state-of-the-art and future perspectives*. Phys
434 Med, 2014. **30**(6): p. 619-34.

- 435 11. Cavanaugh, D., et al., *In vivo respiratory-gated micro-CT imaging in small-animal oncology*
436 *models*. Mol Imaging, 2004. **3**(1): p. 55-62.
- 437 12. Ambrosini, V., et al., *Small animal PET in oncology: the road from bench to bedside*. Cancer
438 Biother Radiopharm, 2009. **24**(2): p. 277-85.
- 439 13. Hoyer, C., et al., *Advantages and challenges of small animal magnetic resonance imaging as a*
440 *translational tool*. Neuropsychobiology, 2014. **69**(4): p. 187-201.
- 441 14. Darne, C., Y. Lu, and E.M. Sevick-Muraca, *Small animal fluorescence and bioluminescence*
442 *tomography: a review of approaches, algorithms and technology update*. Phys Med Biol, 2014.
443 **59**(1): p. R1-64.
- 444 15. Davis, S.C. and K.M. Tichauer, *Small-Animal Imaging Using Diffuse Fluorescence Tomography*.
445 Methods Mol Biol, 2016. **1444**: p. 123-37.
- 446 16. Henriquez, N.V., et al., *Advances in optical imaging and novel model systems for cancer*
447 *metastasis research*. Clin Exp Metastasis, 2007. **24**(8): p. 699-705.
- 448 17. Puaux, A.L., et al., *A comparison of imaging techniques to monitor tumor growth and cancer*
449 *progression in living animals*. Int J Mol Imaging, 2011. **2011**: p. 321538.
- 450 18. Greco, A., et al., *Ultrasound biomicroscopy in small animal research: applications in molecular*
451 *and preclinical imaging*. J Biomed Biotechnol, 2012. **2012**: p. 519238.
- 452 19. Hyvelin, J.M., et al., *Use of ultrasound contrast agent microbubbles in preclinical research:*
453 *recommendations for small animal imaging*. Invest Radiol, 2013. **48**(8): p. 570-83.
- 454 20. Sun, L., et al., *A high-frame rate duplex ultrasound biomicroscopy for small animal imaging in*
455 *vivo*. IEEE Trans Biomed Eng, 2008. **55**(8): p. 2039-49.
- 456 21. Dayton, P.A., et al., *The implementation of acoustic angiography for microvascular and*
457 *angiogenesis imaging*. Annu Int Conf IEEE Eng Med Biol Soc, 2014. **2014**: p. 4283-5.
- 458 22. Newsome, I.G. and P.A. Dayton, *Visualization of Microvascular Angiogenesis Using Dual-*
459 *Frequency Contrast-Enhanced Acoustic Angiography: A Review*. Ultrasound Med Biol, 2020.
460 **46**(10): p. 2625-2635.
- 461 23. Shelton, S.E., et al., *Molecular Acoustic Angiography: A New Technique for High-resolution*
462 *Superharmonic Ultrasound Molecular Imaging*. Ultrasound Med Biol, 2016. **42**(3): p. 769-81.
- 463 24. Wang, L.V. and S. Hu, *Photoacoustic tomography: in vivo imaging from organelles to organs*.
464 Science, 2012. **335**(6075): p. 1458-62.
- 465 25. Wang, L.V. and J. Yao, *A practical guide to photoacoustic tomography in the life sciences*. Nat
466 Methods, 2016. **13**(8): p. 627-38.
- 467 26. Beard, P., *Biomedical photoacoustic imaging*. Interface Focus, 2011. **1**(4): p. 602-31.
- 468 27. Li, M., Y. Tang, and J. Yao, *Photoacoustic tomography of blood oxygenation: A mini review*.
469 Photoacoustics, 2018. **10**: p. 65-73.
- 470 28. Li, M.C., et al., *Sound Out the Deep Colors: Photoacoustic Molecular Imaging at New Depths*.
471 Molecular Imaging, 2020. **19**.
- 472 29. Yao, J.J., et al., *Multiscale photoacoustic tomography using reversibly switchable bacterial*
473 *phytochrome as a near-infrared photochromic probe*. Nature Methods, 2016. **13**(1): p. 67-+.
- 474 30. Gessner, R.C., et al., *Acoustic angiography: a new imaging modality for assessing*
475 *microvasculature architecture*. Int J Biomed Imaging, 2013. **2013**: p. 936593.
- 476 31. Gessner, R.C., S.R. Aylward, and P.A. Dayton, *Mapping Microvasculature with Acoustic*
477 *Angiography Yields Quantifiable Differences between Healthy and Tumor-bearing Tissue*
478 *Volumes in a Rodent Model*. Radiology, 2012. **264**(3): p. 733-740.
- 479 32. Czernuszewicz, T.J., et al., *A new preclinical ultrasound platform for widefield 3D imaging of*
480 *rodents*. Rev Sci Instrum, 2018. **89**(7): p. 075107.
- 481 33. Nishiyama, M., et al., *Ring-array photoacoustic tomography for imaging human finger*
482 *vasculature*. J Biomed Opt, 2019. **24**(9): p. 1-12.

- 483 34. Laufer, J., et al., *Three-dimensional noninvasive imaging of the vasculature in the mouse brain*
484 *using a high resolution photoacoustic scanner*. Appl Opt, 2009. **48**(10): p. D299-306.
- 485 35. Taruttis, A., et al., *Optoacoustic Imaging of Human Vasculature: Feasibility by Using a Handheld*
486 *Probe*. Radiology, 2016. **281**(1): p. 256-63.
- 487 36. Kilian, H.I., et al., *Facile formulation of a long-wavelength cyanine for optical imaging in the*
488 *second near-infrared window*. Biomater Sci, 2020. **8**(15): p. 4199-4205.
- 489 37. Ku, G. and L.V. Wang, *Deeply penetrating photoacoustic tomography in biological tissues*
490 *enhanced with an optical contrast agent*. Opt Lett, 2005. **30**(5): p. 507-9.
- 491 38. Zhang, Q., et al., *Gold nanoparticles as a contrast agent for in vivo tumor imaging with*
492 *photoacoustic tomography*. Nanotechnology, 2009. **20**(39): p. 395102.
- 493 39. Bosschaart, N., et al., *A literature review and novel theoretical approach on the optical*
494 *properties of whole blood*. Lasers Med Sci, 2014. **29**(2): p. 453-79.
- 495 40. Luke, G.P., D. Yeager, and S.Y. Emelianov, *Biomedical applications of photoacoustic imaging with*
496 *exogenous contrast agents*. Ann Biomed Eng, 2012. **40**(2): p. 422-37.
- 497 41. Demitri, C., et al., *Hydrogel based tissue mimicking phantom for in-vitro ultrasound contrast*
498 *agents studies*. J Biomed Mater Res B Appl Biomater, 2008. **87**(2): p. 338-45.
- 499 42. Huang, Q., et al., *Intravital imaging of mouse embryos*. Science, 2020. **368**(6487): p. 181-186.
- 500 43. Mu, J.W., et al., *In vivo quantification of embryonic and placental growth during gestation in*
501 *mice using micro-ultrasound*. Reproductive Biology and Endocrinology, 2008. **6**.
- 502 44. Roberts, V.H.J. and A.E. Frias, *Contrast-enhanced ultrasound for the assessment of placental*
503 *development and function*. Biotechniques, 2020. **69**(5): p. 392-399.
- 504 45. Preisser, S., et al., *Vessel orientation-dependent sensitivity of optoacoustic imaging using a linear*
505 *array transducer*. J Biomed Opt, 2013. **18**(2): p. 26011.
- 506 46. Mishra, K., et al., *Multiplexed whole-animal imaging with reversibly switchable optoacoustic*
507 *proteins*. Sci Adv, 2020. **6**(24): p. eaaz6293.
- 508 47. Wang, Y.H., et al., *Review of methods to improve the performance of linear array-based*
509 *photoacoustic tomography*. Journal of Innovative Optical Health Sciences, 2020. **13**(2).
- 510 48. Xia, J., et al., *Three-dimensional photoacoustic tomography based on the focal-line concept*. J
511 Biomed Opt, 2011. **16**(9): p. 090505.
- 512 49. Fehm, T.F., et al., *In vivo whole-body optoacoustic scanner with real-time volumetric imaging*
513 *capacity*. Optica, 2016. **3**(11): p. 1153-1159.
- 514 50. Wu, Y.L., et al., *Emerging contrast agents for multispectral optoacoustic imaging and their*
515 *biomedical applications*. Chemical Society Reviews, 2021. **50**(14): p. 7924-7940.
- 516 51. Mattes, D., et al., *PET-CT image registration in the chest using free-form deformations*. IEEE
517 Transactions on Medical Imaging, 2003. **22**(1): p. 120-128.
- 518 52. Streeter, J.E., et al., *Improving sensitivity in ultrasound molecular imaging by tailoring contrast*
519 *agent size distribution: in vivo studies*. Mol Imaging, 2010. **9**(2): p. 87-95.
- 520 53. Shashank Sirsi, J.F., Mark Borden, Shunichi Homma, *High-frequency ultrasound imaging of size-*
521 *isolated microbubbles in mice*. IEEE International Ultrasonics Symposium Proceedings, 2009. **20-**
522 **23**(Sept. 2009).
- 523 54. Feshitan, J.A., et al., *Microbubble size isolation by differential centrifugation*. J Colloid Interface
524 Sci, 2009. **329**(2): p. 316-24.
- 525 55. Kimmel, E., *Cavitation bioeffects*. Crit Rev Biomed Eng, 2006. **34**(2): p. 105-61.
- 526 56. Yuan, F., C. Yang, and P. Zhong, *Cell membrane deformation and bioeffects produced by tandem*
527 *bubble-induced jetting flow*. Proc Natl Acad Sci U S A, 2015. **112**(51): p. E7039-47.
- 528 57. Annemieke van Wamel, A.B., Folkert ten Cate, Nico de Jong, *Effects of Diagnostic Ultrasound*
529 *Parameters on Molecular Uptake and Cell Viability*. Proceedings of the International Ultrasonics
530 Symposium, 2002. **8-11**(October 2002).

- 531 58. Xie, F., et al., *Effects of transcranial ultrasound and intravenous microbubbles on blood brain*
532 *barrier permeability in a large animal model*. *Ultrasound Med Biol*, 2008. **34**(12): p. 2028-34.
- 533 59. Bayer, C.L., et al., *Ultrasound-guided spectral photoacoustic imaging of hemoglobin oxygenation*
534 *during development*. *Biomed Opt Express*, 2017. **8**(2): p. 757-763.
- 535 60. Basak, K., et al., *Non-invasive determination of murine placental and foetal functional*
536 *parameters with multispectral optoacoustic tomography*. *Light Sci Appl*, 2019. **8**: p. 71.
- 537 61. Huda, K., et al., *Spherical-view photoacoustic tomography for monitoring in vivo placental*
538 *function*. *Photoacoustics*, 2020. **20**: p. 100209.
- 539 62. Woods, L., V. Perez-Garcia, and M. Hemberger, *Regulation of Placental Development and Its*
540 *Impact on Fetal Growth-New Insights From Mouse Models*. *Frontiers in Endocrinology*, 2018. **9**.
- 541 63. Turner, R.J. and B.A. Carroll, *Ultrasound appearance of decidual reaction in the uterus during*
542 *normal pregnancy*. *AJR Am J Roentgenol*, 1979. **133**(3): p. 493-6.
- 543 64. Cross, J.C., et al., *Branching morphogenesis during development of placental villi*. *Differentiation*,
544 2006. **74**(7): p. 393-401.
- 545 65. Chomas, J.E., et al., *Threshold of fragmentation for ultrasonic contrast agents*. *J Biomed Opt*,
546 2001. **6**(2): p. 141-50.
- 547 66. Newsome, I.G., T.M. Kierski, and P.A. Dayton, *Assessment of the Superharmonic Response of*
548 *Microbubble Contrast Agents for Acoustic Angiography as a Function of Microbubble Parameters*.
549 *Ultrasound Med Biol*, 2019. **45**(9): p. 2515-2524.
- 550 67. Lasso, A., et al., *PLUS: open-source toolkit for ultrasound-guided intervention systems*. *IEEE Trans*
551 *Biomed Eng*, 2014. **61**(10): p. 2527-37.
- 552 68. Xu, M. and L.V. Wang, *Universal back-projection algorithm for photoacoustic computed*
553 *tomography*. *Phys Rev E Stat Nonlin Soft Matter Phys*, 2005. **71**(1 Pt 2): p. 016706.
- 554 69. Wang, Z., J. Li, and R. Wu, *Time-delay- and time-reversal-based robust Capon beamformers for*
555 *ultrasound imaging*. *IEEE Trans Med Imaging*, 2005. **24**(10): p. 1308-22.
- 556 70. Li, L., et al., *Small near-infrared photochromic protein for photoacoustic multi-contrast imaging*
557 *and detection of protein interactions in vivo*. *Nat Commun*, 2018. **9**(1): p. 2734.

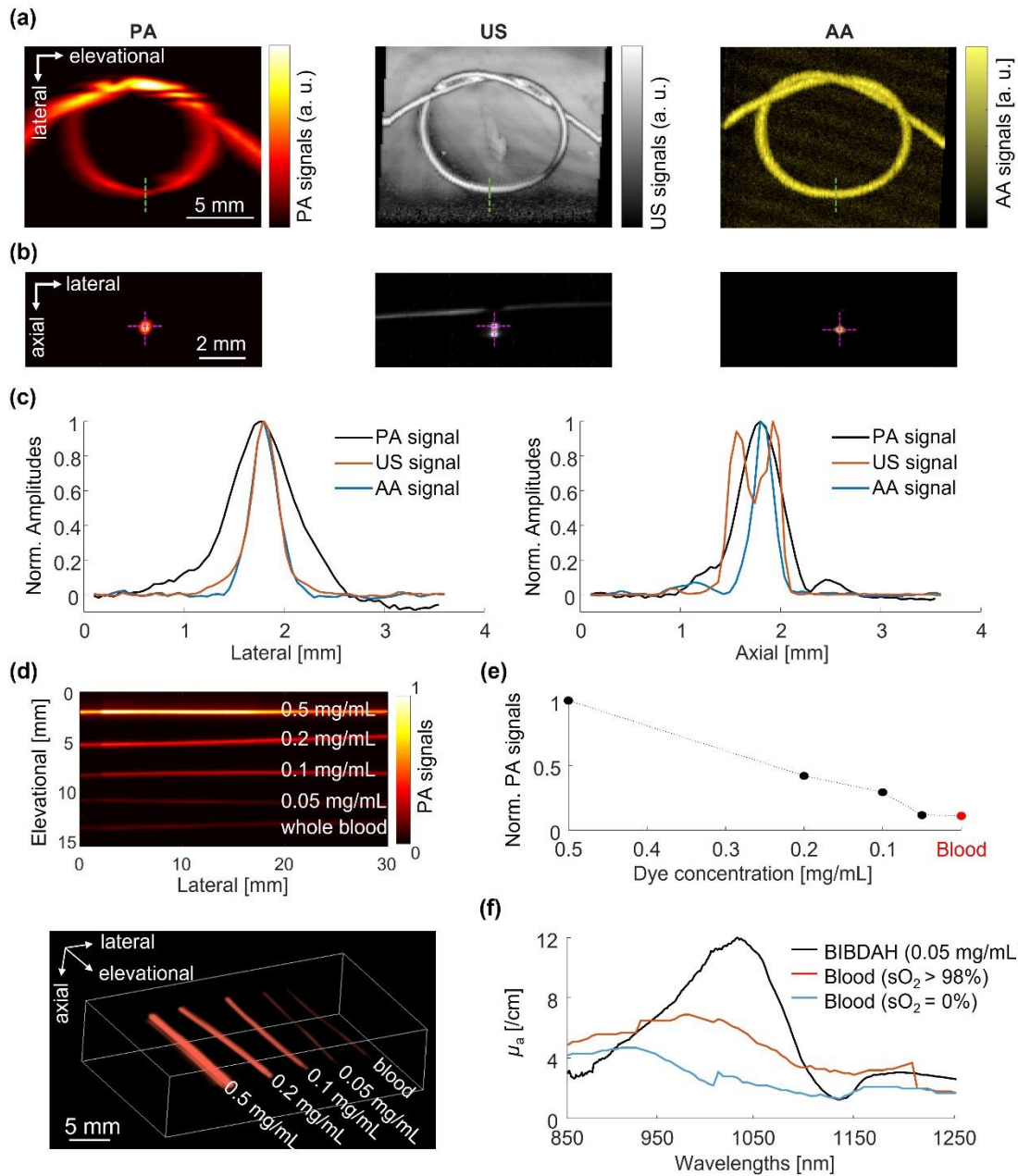


558

559 **Figure 1. Integrated photoacoustic, ultrasound and angiographic tomography (PAUSAT).**

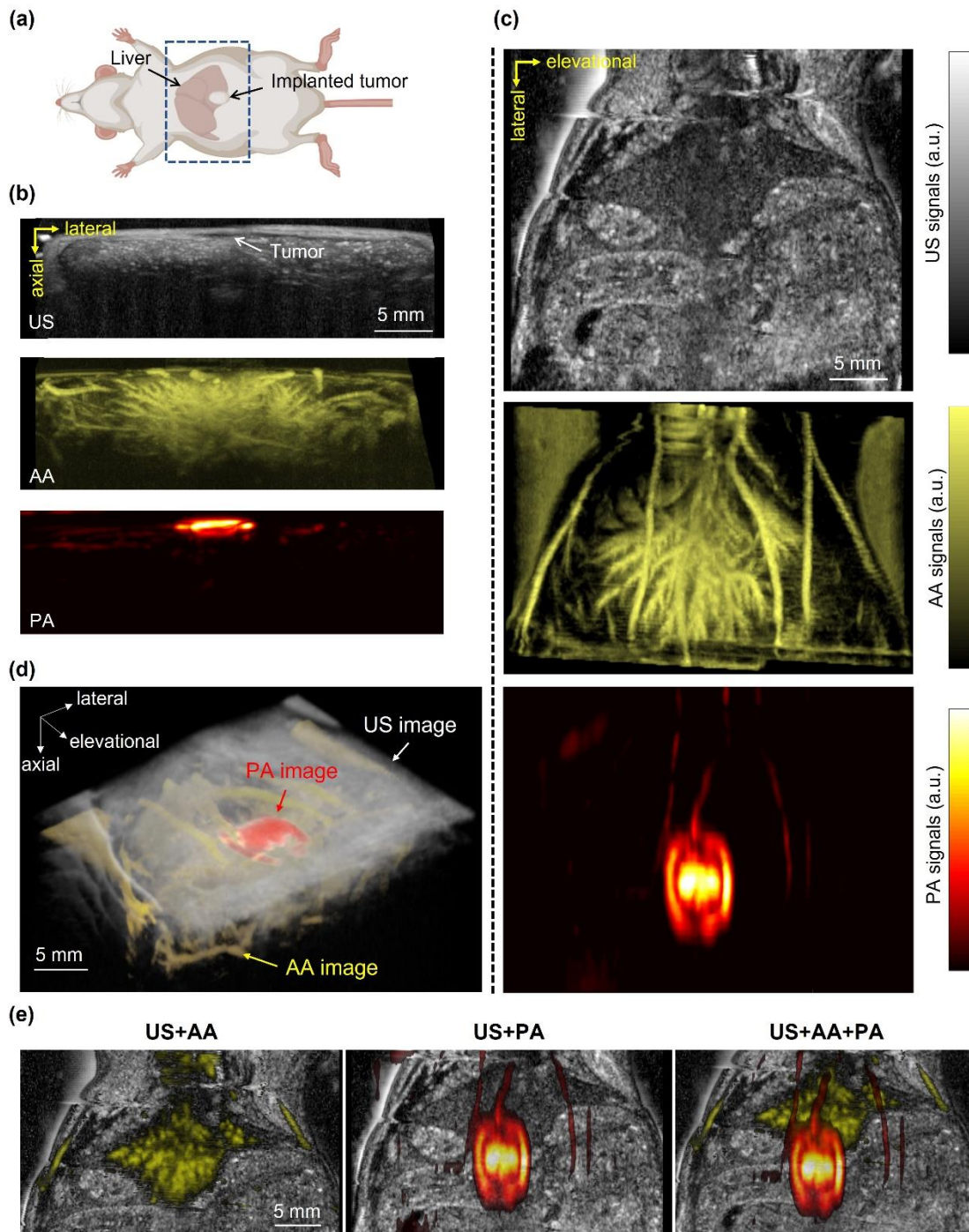
560 (a) Schematic of the PAUSAT system, showing the key acoustic, optical and mechanical
 561 components. (b) Imaging principles of the PA, US, and AA modes. In the PA mode, the pulsed
 562 laser light is delivered by the optical fiber bundle and the resultant acoustic waves are detected
 563 by the linear transducer array; In the US mode, the high-frequency inner-element of the focused
 564 wobbler transducer transmits the acoustic waves and detects the reflected echo signals; In the AA
 565 mode, the low-frequency outer-element of the wobbler transmits a strong acoustic pulse to burst
 566 the flowing microbubbles in the blood vessels, and the high-frequency inner-elements detects the

567 bursting signals from the bubbles. (c) Spatial resolution measurement of the PA mode. (d)
 568 Spatial resolution measurement of the US mode. (e) Comparison of the penetration depth of the
 569 US mode at three different frequencies.



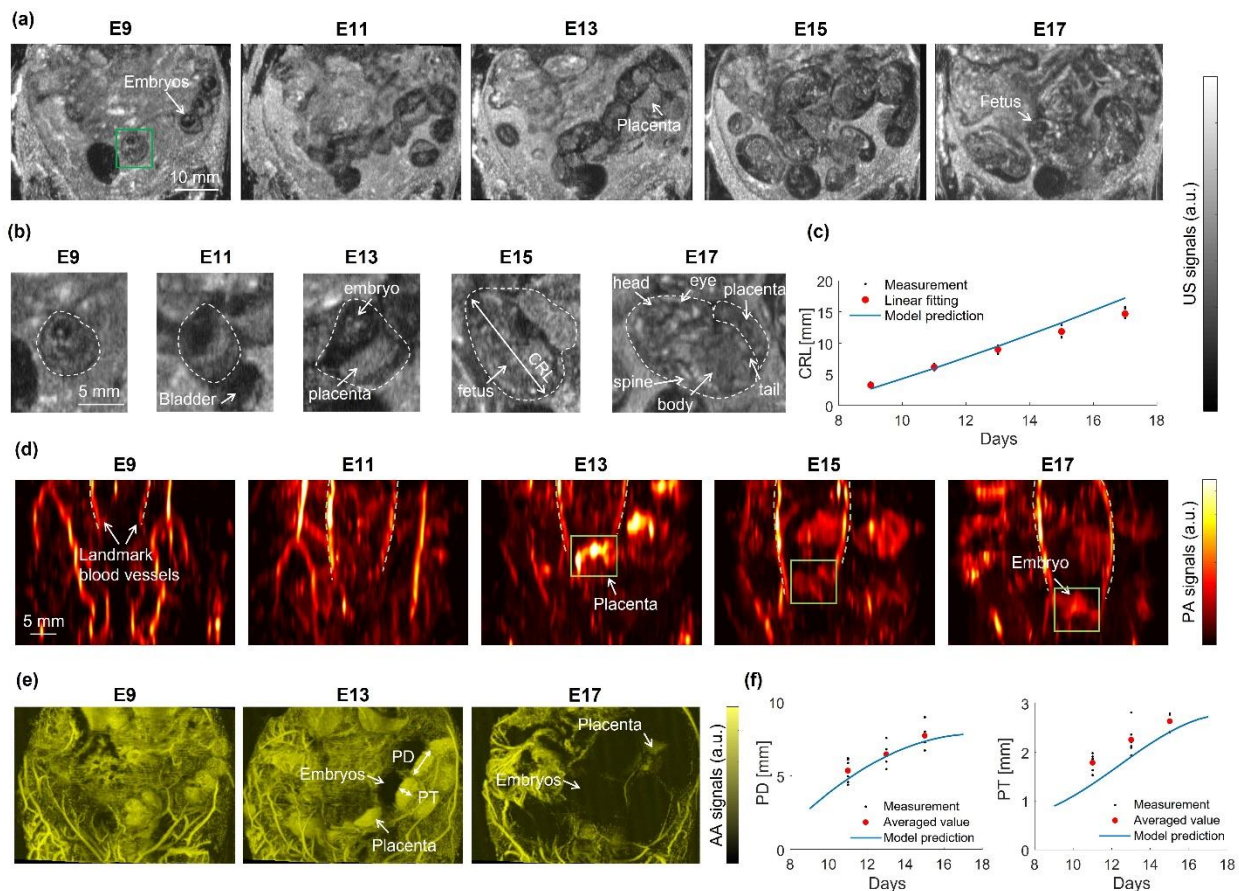
570
 571 **Fig. 2. PAUSAT system validation on phantoms.** (a) Images of a tube knot filled with
 572 BIBDAH, water, and microbubbles with PA, US, and AA, respectively. (b) Cross-sectional
 573 images of the tube along the green-dotted lines in (a). (c) Lateral and axial signal profiles along
 574 the magenta dotted lines in (b). (d) Top-view projection PA image and 3D rendering of tubes

575 filled with blood and BIBDAH dye at different concentrations. (e) Quantitative PA signals from
 576 blood and dyes. (f) Optical absorption spectra of BIBDAH at 50 $\mu\text{g/ml}$, oxygenated and
 577 deoxygenated blood.



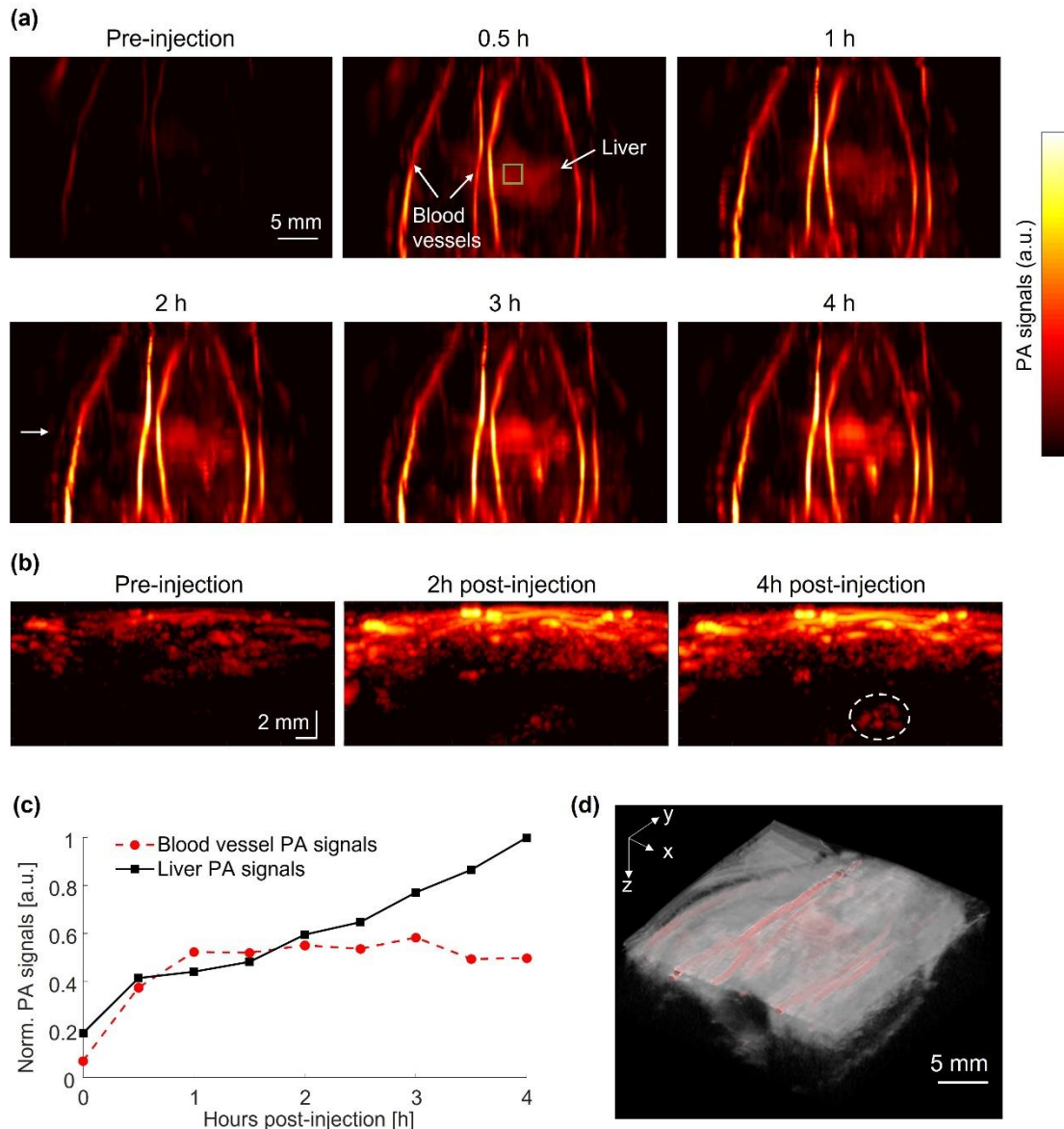
578
 579 **Fig. 3. PAUSAT system validation on small animals.** (a) The implantation position of the
 580 BIBDAH dye mixed Matrigel tumor. (b) Axial cross-sectional images of the mouse liver region

581 by the PA, US, and AA mode. (c) Coronal images of the liver region by the PA, US, and AA
 582 mode. US shows one slice where the liver was located while AA and PA show the maximum
 583 amplitude projections. (d) Three-dimensional rendering of the superimposed PA (in hot color),
 584 US (in gray color), and AA (in yellow color) images. (e) Superimposed images of different
 585 imaging modes showing the relative positions of the targets.



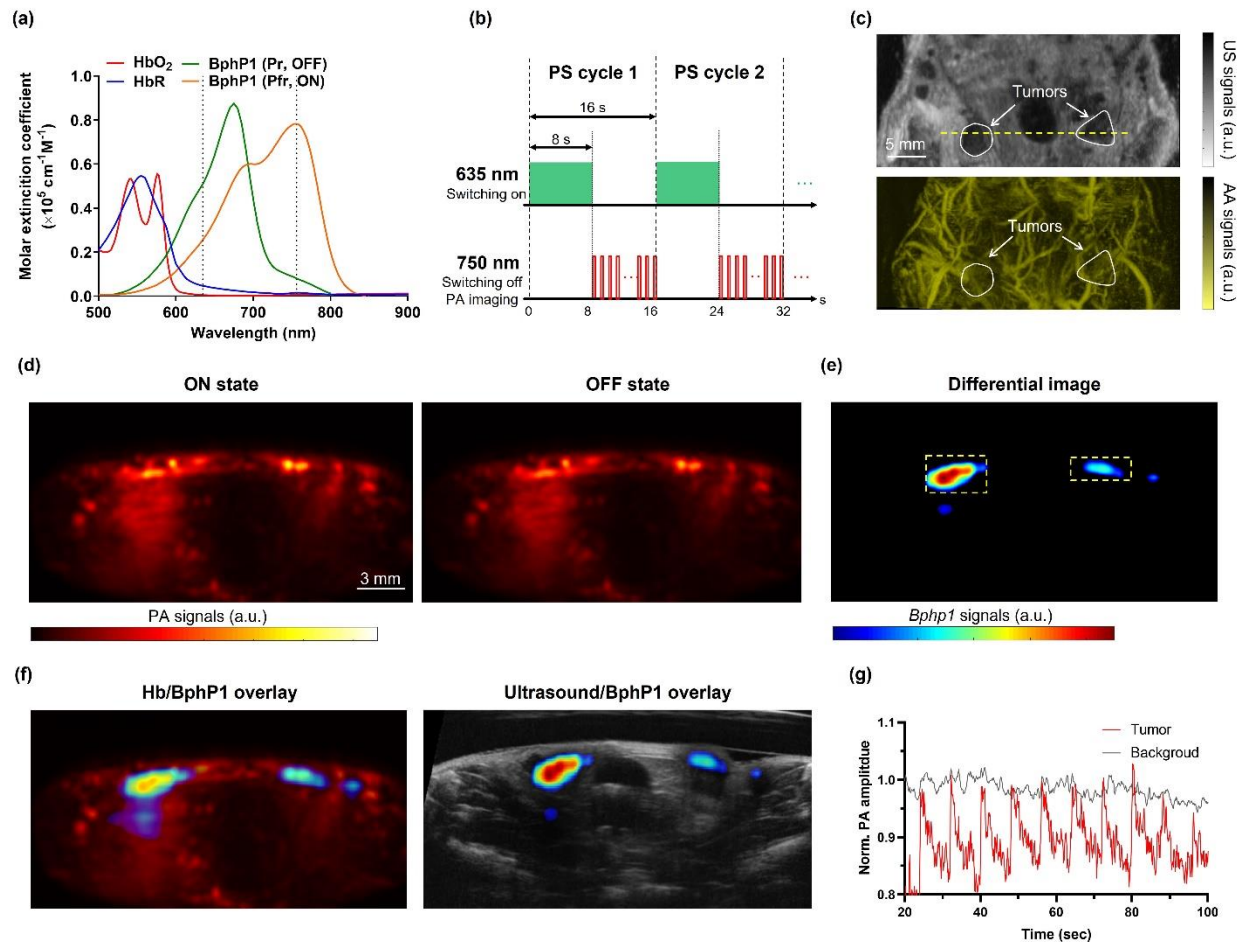
586

587 **Fig 4. Longitudinal imaging of mouse pregnancy by PAUSAT.** (a) Longitudinal US images
 588 of a pregnant mouse at E9, E11, E13, E15 and E17. (b) Close-up images of a single embryo from
 589 E9 to E17. (c) Embryo's crown-rump length measured from the US images (black dots), the
 590 linear fitting (red dots), and the model prediction (blue curve). (d) Longitudinal PA images of the
 591 pregnant mouse. (e) Longitudinal AA images of the maternal vasculature and placentas. (f)
 592 Placental diameter (PD) and placental thickness (PT) measurements from the US and AA images
 593 for individual embryos (black dots), the averaged values (red dots), and the model prediction
 594 (blue curves).



595

596 **Fig. 5. Tracking the biodistribution of an NIR-II dye.** (a) PA images of the mouse liver region
 597 before and after the injection of an NIR-II dye BIBDAH. (b) Axial cross-sectional images of the
 598 liver region indicated by the white arrow in (a). (c) PA signal dynamics in the major blood
 599 vessels and in the liver region as indicated by the green square in (a). (d) 3D rendering of the
 600 superimposed US (shown in gray) and PA (shown in color) image of the mouse 4 hours post-
 601 injection.



602

603 **Fig. 6. Detecting reversibly photoswitching tumor *in vivo*.** (a) Molecular extinction
 604 coefficients of oxygenated hemoglobin (HbO₂, red curve), deoxygenated hemoglobin (Hb, blue
 605 curve), ON state *Bphp1* (orange curve) and OFF state *Bphp1* (green curve) from 500 nm to 900
 606 nm. (b) PA laser excitation sequence used for photoacoustic imaging and photoswitching *Bphp1*.
 607 The PA images were acquired at 750 nm. (c) Coronal-view US and AA images of the mouse
 608 tumor region. The circles indicate the positions of implanted tumors. (d) Axial cross-sectional
 609 PA images at the ON and OFF state of the *Bphp1* tumor. The position of the cross-section is
 610 indicated in the US image in (c). (e) Differential PA image between the ON and OFF state,
 611 showing the tumor only. (f) The differential image overlaid with PA and US images. (g) PA
 612 signal changes from tumor and blood over multiple photoswitching cycles.

613

Figures

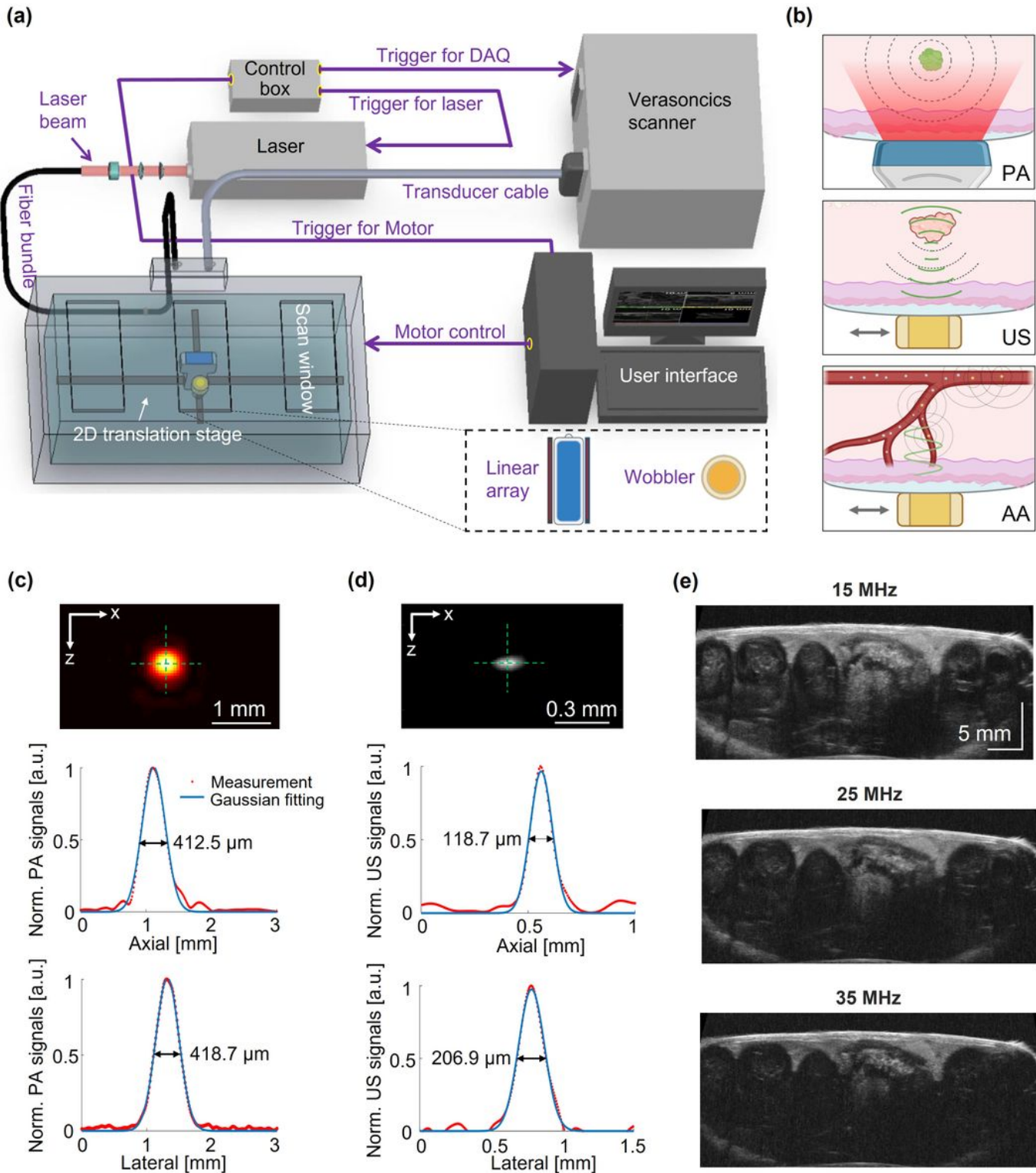


Figure 1

Integrated photoacoustic, ultrasound and angiographic tomography (PAUSAT). (a) Schematic of the PAUSAT system, showing the key acoustic, optical and mechanical components. (b) Imaging principles of the PA, US, and AA modes. In the PA mode, the pulsed laser light is delivered by the optical fiber bundle

and the resultant acoustic waves are detected by the linear transducer array; In the US mode, the high-frequency inner-element of the focused wobbler transducer transmits the acoustic waves and detects the reflected echo signals; In the AA mode, the low-frequency outer-element of the wobbler transmits a strong acoustic pulse to burst the flowing microbubbles in the blood vessels, and the high-frequency inner-elements detects the bursting signals from the bubbles. (c) Spatial resolution measurement of the PA mode. (d) Spatial resolution measurement of the US mode. (e) Comparison of the penetration depth of the US mode at three different frequencies.

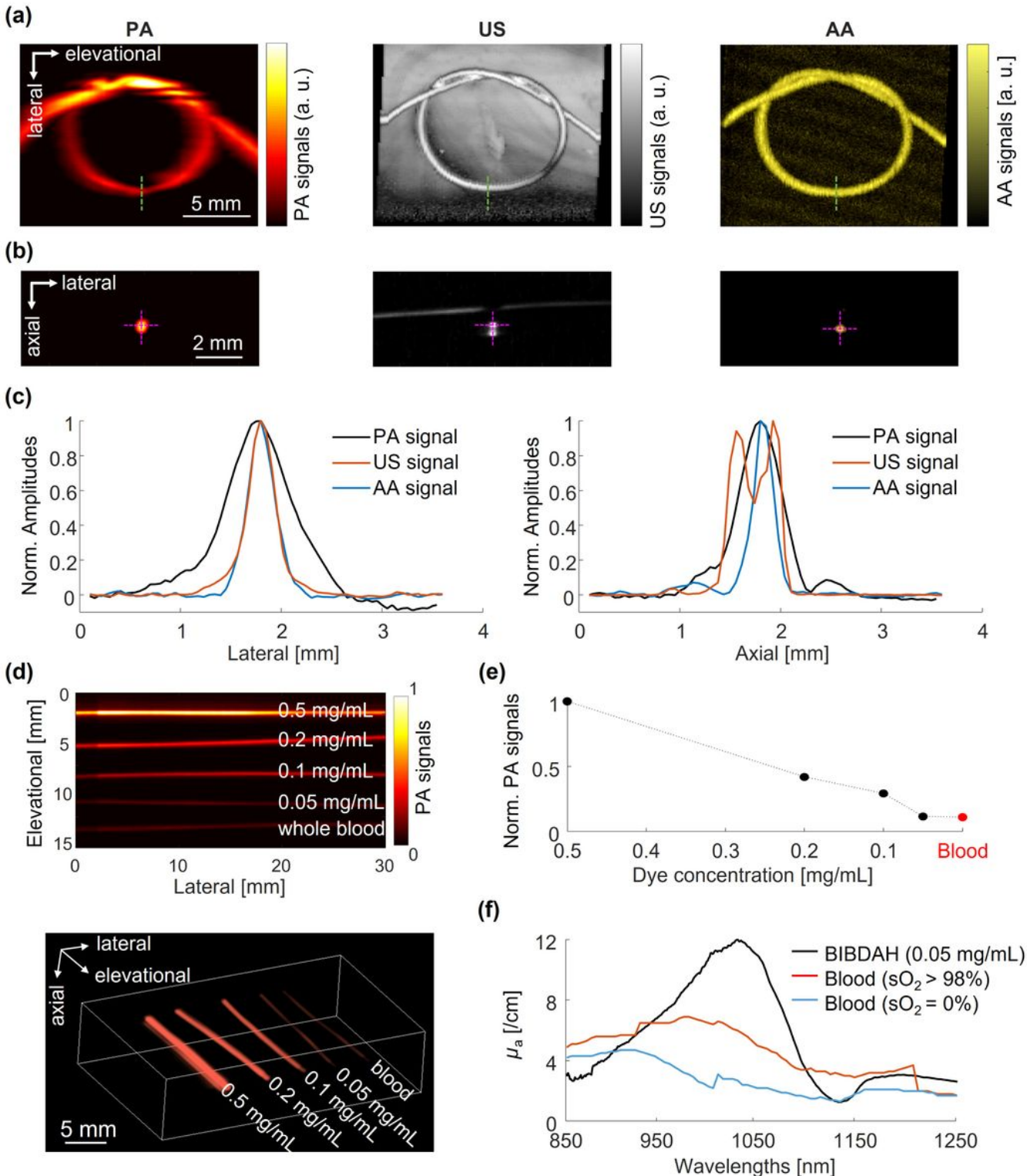


Figure 2

PAUSAT system validation on phantoms. (a) Images of a tube knot filled with BIBDAH, water, and microbubbles with PA, US, and AA, respectively. (b) Cross-sectional images of the tube along the green-dotted lines in (a). (c) Lateral and axial signal profiles along the magenta dotted lines in (b). (d) Top-view projection PA image and 3D rendering of tubes filled with blood and BIBDAH dye at different concentrations. (e) Quantitative PA signals from blood and dyes. (f) Optical absorption spectra of BIBDAH at 50 $\mu\text{g/ml}$, oxygenated and deoxygenated blood.

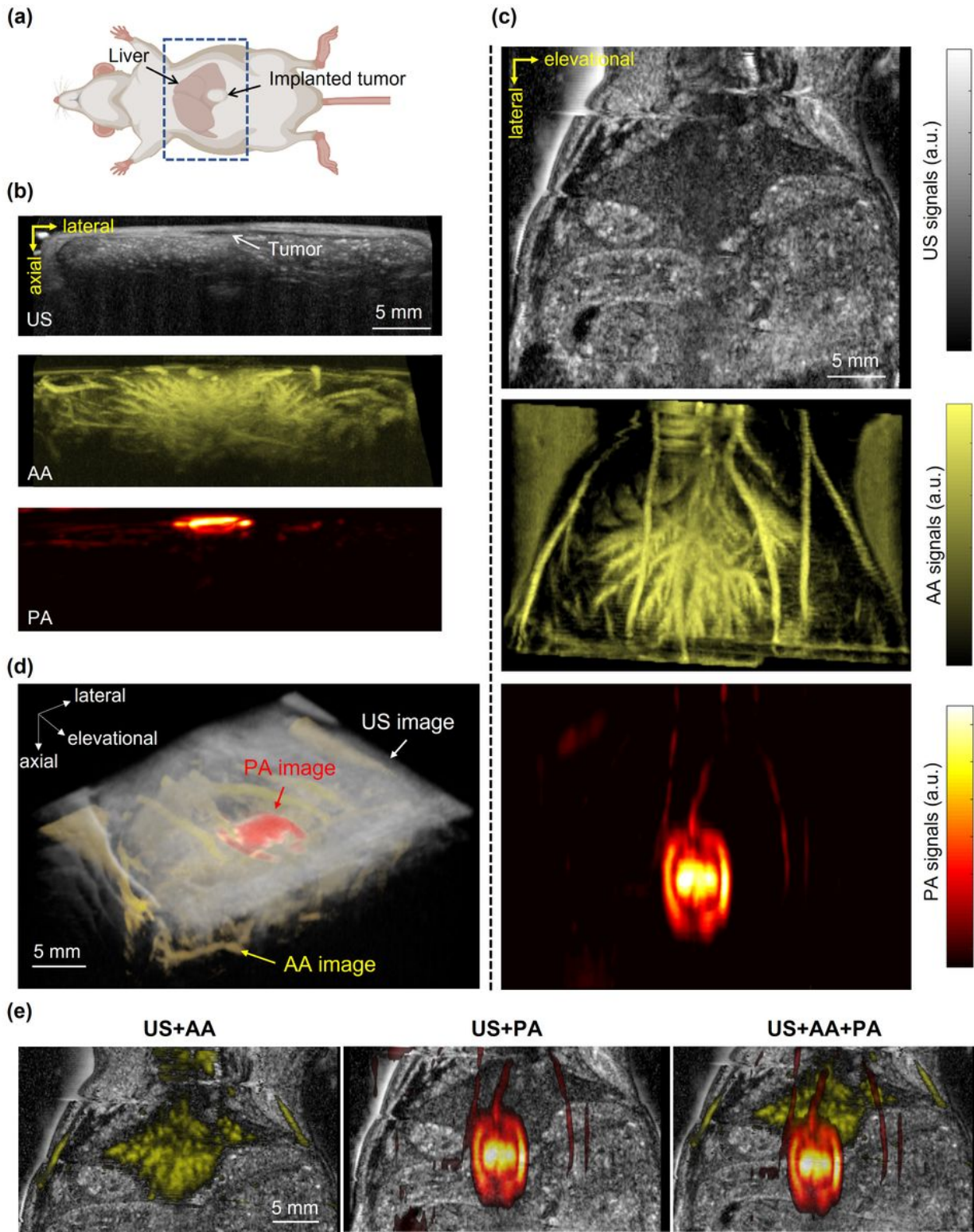


Figure 3

PAUSAT system validation on small animals. (a) The implantation position of the BIBDAH dye mixed Matrigel tumor. (b) Axial cross-sectional images of the mouse liver region by the PA, US, and AA mode. (c) Coronal images of the liver region by the PA, US, and AA mode. US shows one slice where the liver was located while AA and PA show the maximum amplitude projections. (d) Three-dimensional rendering of

the superimposed PA (in hot color), US (in gray color), and AA (in yellow color) images. (e) Superimposed images of different imaging modes showing the relative positions of the targets.

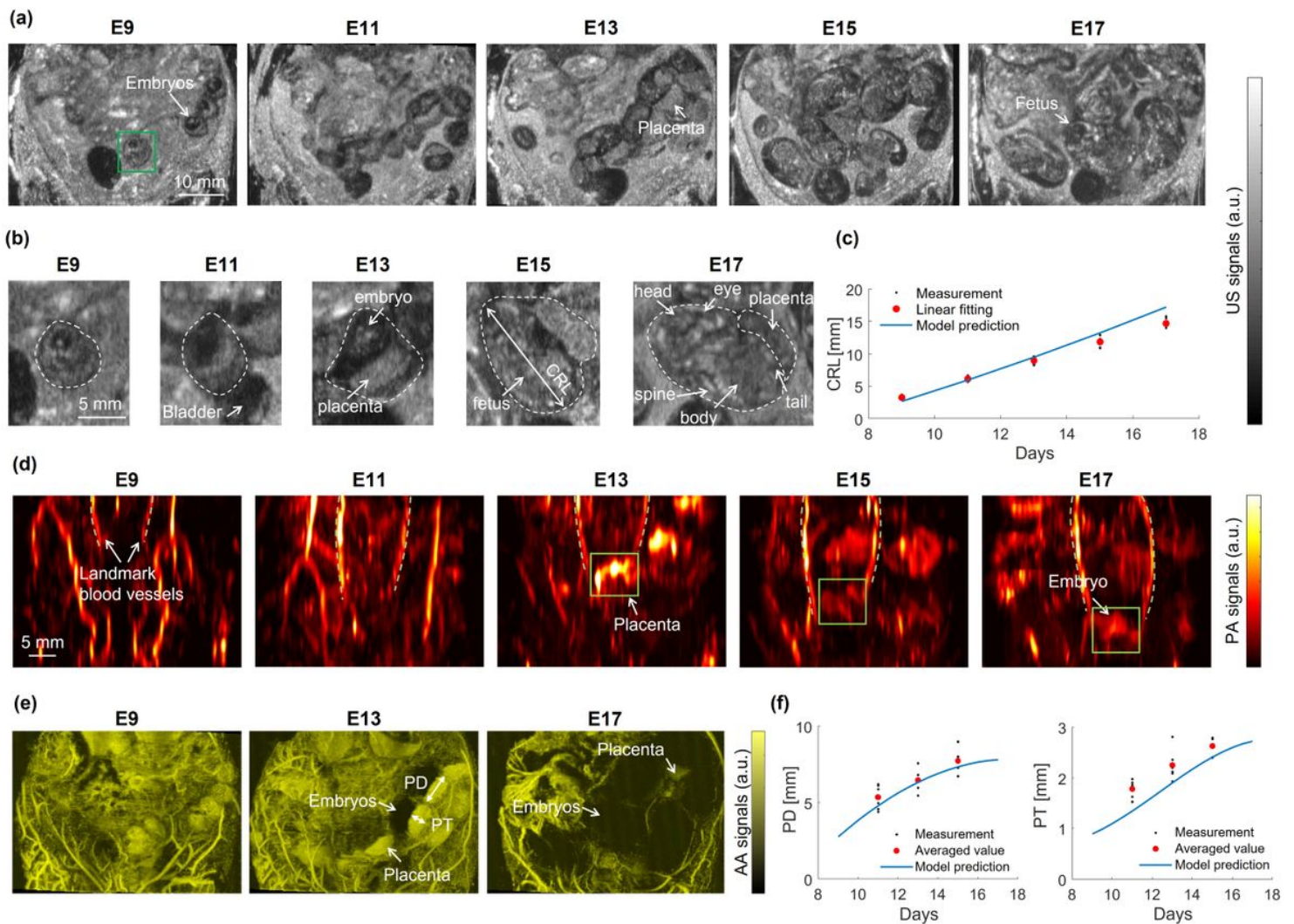


Figure 4

(a) Longitudinal US images of a pregnant mouse at E9, E11, E13, E15 and E17. (b) Close-up images of a single embryo from E9 to E17. (c) Embryo's crown-rump length measured from the US images (black dots), the linear fitting (red dots), and the model prediction (blue curve). (d) Longitudinal PA images of the pregnant mouse. (e) Longitudinal AA images of the maternal vasculature and placentas. (f) Placental diameter (PD) and placental thickness (PT) measurements from the US and AA images for individual embryos (black dots), the averaged values (red dots), and the model prediction (blue curves).

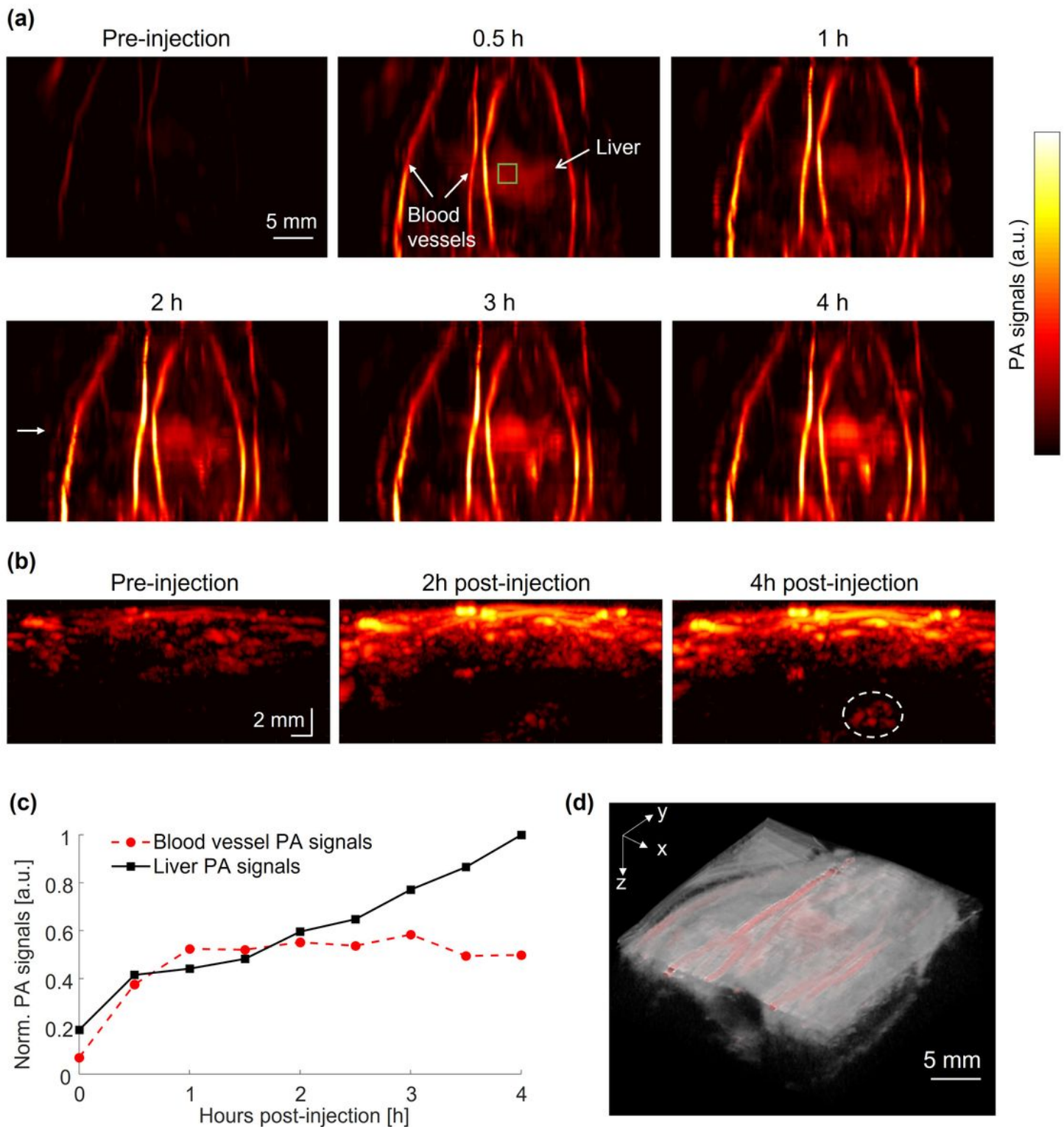


Figure 5

Tracking the biodistribution of an NIR-II dye. (a) PA images of the mouse liver region before and after the injection of an NIR-II dye BIBDAH. (b) Axial cross-sectional images of the liver region indicated by the white arrow in (a). (c) PA signal dynamics in the major blood vessels and in the liver region as indicated by the green square in (a). (d) 3D rendering of the superimposed US (shown in gray) and PA (shown in color) image of the mouse 4 hours post-injection.

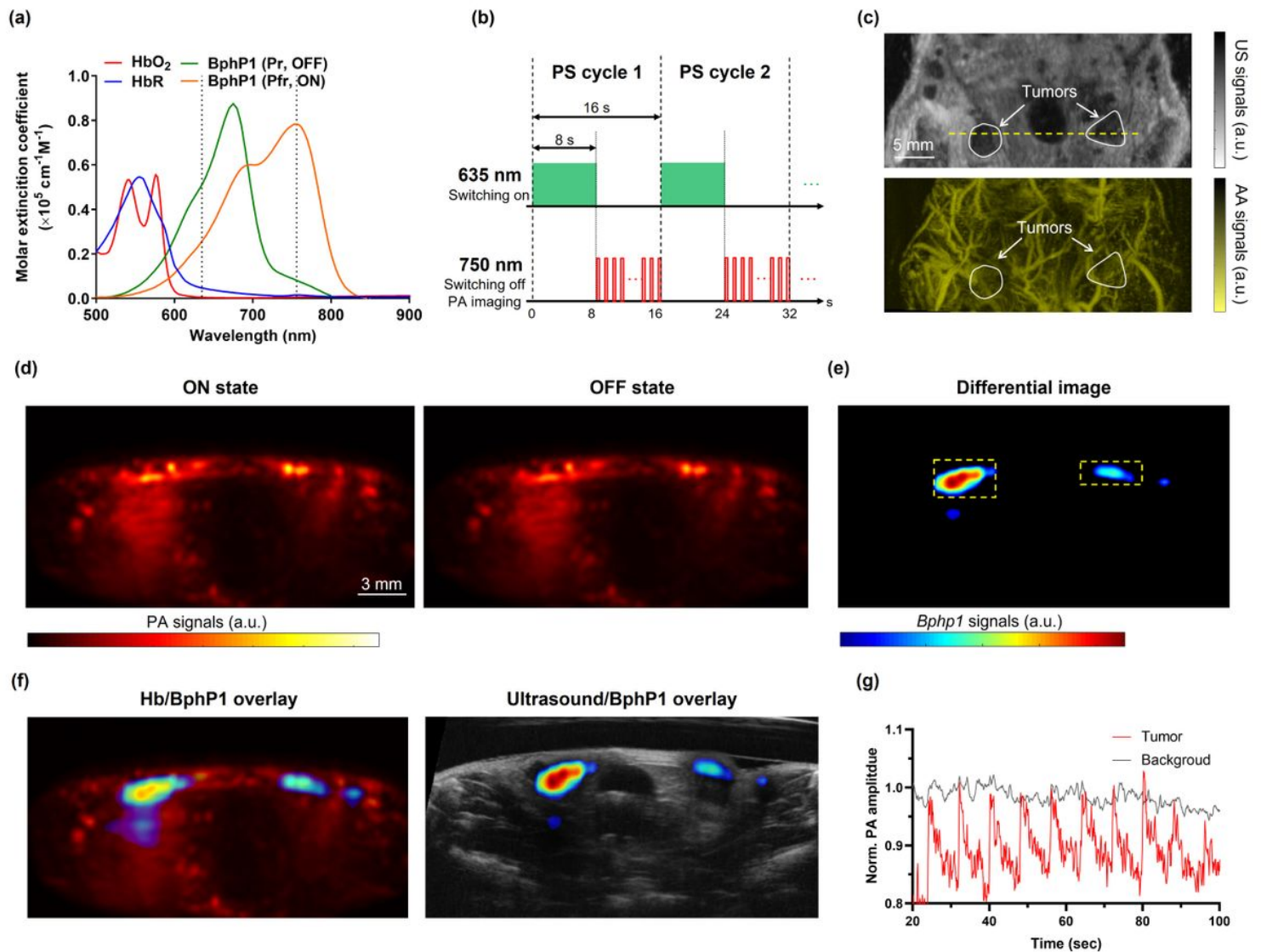


Figure 6

Detecting reversibly photoswitching tumor in vivo. (a) Molecular extinction coefficients of oxygenated hemoglobin (HbO₂, red curve), deoxygenated hemoglobin (Hb, blue curve), ON state Bphp1 (orange curve) and OFF state Bphp1 (green curve) from 500 nm to 900 nm. (b) PA laser excitation sequence used for photoacoustic imaging and photoswitching Bphp1. The PA images were acquired at 750 nm. (c) Coronal-view US and AA images of the mouse tumor region. The circles indicate the positions of implanted tumors. (d) Axial cross-sectional PA images at the ON and OFF state of the Bphp1 tumor. The position of the cross-section is indicated in the US image in (c). (e) Differential PA image between the ON and OFF state, showing the tumor only. (f) The differential image overlaid with PA and US images. (g) PA signal changes from tumor and blood over multiple photoswitching cycles.

Supplementary Files

This is a list of supplementary files associated with this preprint. Click to download.

- [Supplementary1Wobberscanning.mp4](#)
- [Supplementary2AnimalValidation.mp4](#)
- [Supplementary3PregnantMouseUSimages.mp4](#)
- [Supplementary4PregnantMousePAimages.mp4](#)
- [Supplementary5PregnantMouseAAimages.mp4](#)
- [Supplementary6PregnantMouseAA.mp4](#)